

# Interstellar oxygen along the line of sight of Cygnus X-2

I. Psaradaki<sup>1,2</sup>, E. Costantini<sup>1,2</sup>, M. Mehdipour<sup>1</sup>, D. Rogantini<sup>1,2</sup>, C. P. de Vries<sup>1</sup>, F. de Groot<sup>3</sup>, H. Mutschke<sup>4</sup>, S. Trasobares<sup>5</sup>, L.B.F.M. Waters<sup>1,2</sup>, and S.T. Zeegers<sup>6</sup>

<sup>1</sup> SRON Netherlands Institute for Space Research, Sorbonnelaan 2, 3584 CA Utrecht, the Netherlands  
e-mail: I.Psaradaki@sron.nl

<sup>2</sup> Anton Pannekoek Astronomical Institute, University of Amsterdam, P.O. Box 94249, 1090 GE Amsterdam, the Netherlands

<sup>3</sup> Debye Institute for Nanomaterials Science, Utrecht University, Universiteitsweg 99, 3584 CG Utrecht, Netherlands

<sup>4</sup> Astrophysikalisches Institut und Universitäts-Sternwarte (AIU), Schillergäßchen 2-3, 07745 Jena, Germany

<sup>5</sup> Ciencia de los Materiales e Ingeniería Metalúrgica y Química Inorgánica, Universidad de Cadiz

<sup>6</sup> Academia Sinica, Institute of Astronomy and Astrophysics, 11F Astronomy-Mathematics Building, NTU/AS campus, No. 1, Section 4, Roosevelt Rd., Taipei 10617, Taiwan

January 20, 2022

## ABSTRACT

Interstellar dust permeates our Galaxy and plays an important role in many physical processes in the diffuse and dense regions of the interstellar medium. High-resolution X-ray spectroscopy, coupled with modelling based on laboratory dust measurements, provides a unique probe to investigate the interstellar dust properties along our line of sight towards Galactic X-ray sources. Here, we focus on the oxygen content of the interstellar medium through its absorption features in the X-ray spectra. To model the dust features, we perform a laboratory experiment using the electron microscope facility located at the University of Cadiz in Spain, where we acquire new laboratory data in the oxygen K-edge. We study 18 dust samples of silicates and oxides with different chemical compositions. The laboratory measurements are adopted for our astronomical data analysis. We carry out a case study on the X-ray spectrum of the bright low-mass X-ray binary Cygnus X-2, observed by XMM-Newton. We determine different temperature phases of the ISM, and parameterize oxygen in both gas (neutral and ionised) and dust form. We find Solar abundances of oxygen along the line of sight towards the source. Due to both the relatively low depletion of oxygen into dust form and the shape of the oxygen cross section profiles, it is challenging to determine the precise chemistry of interstellar dust. However, silicates provide an acceptable fit. Finally, we discuss the systematic discrepancies in the atomic (gaseous phase) data of the oxygen edge spectral region using different X-ray atomic databases, and also consider future prospects for studying the ISM with the Arcus concept mission.

**Key words.** astrochemistry, X-rays: binaries, ISM:dust

## 1. Introduction

The composition of the interstellar medium (ISM) is very important for the evolution of the Galaxy and for star formation processes. In particular, interstellar dust (ID) is an important constituent of our Galaxy as it can control the temperature of the ISM and it is the catalyst for the formation of complex molecules (Mathis 1990).

The dust chemical and physical properties in the diffuse ISM are not yet fully understood. Observations show that ID in the diffuse ISM is not spatially homogeneous (e.g. Planck Collaboration 2011b, Planck Collaboration 2011a, Ysard et al. 2015). Silicate grains are an important and abundant component of ID and can be found in many different stages of the life cycle of stars (Henning 2010). It is believed to be mainly produced in oxygen-rich asymptotic giant branch stars (Gail et al. 2009) but also in novae and supernovae type II (Wooden et al. 1993, Rho et al. 2008) and young stellar objects (Nittler et al. 1997). On the other hand, carbonaceous grains could form in interstellar clouds, as carbon grains likely have shorter lifetimes (Jones & Nuth 2011).

The physical and chemical properties of silicate dust have been historically studied along different directions in the Galaxy at wavelengths ranging from radio to the ultraviolet (Draine & Li 2001, Dwek et al. 2004). It is believed that the elements such as

O, Fe, Si and Mg form the cosmic silicates, which represent most of the dust mass in the ISM (Mathis 1998). Another evidence for such elements to be locked up in dust is given by the fact that they are depleted from the gaseous phase (Henning 2010, Savage & Sembach 1996, Jenkins 2009).

Oxygen is one of the most abundant and important elements for life on Earth. However, the total budget of oxygen in the diffuse and dense interstellar media cannot be fully explained yet (Whittet 2010). Jenkins (2009) reported that the oxygen in the diffuse interstellar gas is being depleted at a rate that cannot be associated with only silicates and metallic oxides. They found that the total fraction of the missing oxygen is not compatible with the stoichiometric ratios of even the most oxygen rich silicate compounds. This requires some contribution of additional compounds.

It has also been proposed that oxygen must be locked up in molecules, together with elements with a high cosmic abundance such as CO, CO<sub>2</sub> and O<sub>2</sub> (Jenkins 2009). These oxygen-bearing molecules have small but not negligible abundance (van Dishoeck 2004). Also, van Dishoeck et al. (1998) found that close to young stellar objects, for large extinction values, oxygen atoms are found in the form of water. Whittet et al. (1988), Eiroa & Hodapp (1989) and Smith et al. (1993) found that the strength of the 3.05  $\mu\text{m}$  water ice feature becomes much weaker as the extinction decreases. Later on, Whittet et al. (2001) showed that

the same feature becomes detectable for extinction larger than 3.2 and increases linearly with increasing extinction above that value.

High-resolution X-ray spectroscopy is a powerful tool to unveil the physical and chemical properties of the diffuse interstellar medium (Wilms et al. 2000, Lee & Ravel 2005, Lee 2009, de Vries & Costantini 2009, Pinto et al. 2013, Corrales et al. 2016, Schulz et al. 2016, Zeegers et al. 2017, 2019, Rogantini et al. 2018). It provides the possibility to study the composition of cosmic dust in different environments of the ISM through the study of absorption features of gas and dust. In particular, the X-ray Absorption Fine Structures (XAFS) are unique fingerprints of dust. When an X-ray photon excites a core electron ( $n=1$ ), the outwardgoing photo-electron will interact with the neighboring atoms. This interaction will modify the wave function of the photo-electron due to constructive and destructive interferences. In this way, the absorption probability will be modified in a unique pattern which depends on the configuration of the neighboring atoms. Therefore, the shape of XAFS can be used to determine the chemical structure of dust (see also Newville (2004) for further explanation).

The oxygen K-edge region has been previously explored using observations from the XMM-Newton and the Chandra satellites. Costantini et al. (2012), Pinto et al. (2010) found that about 15-25 % of the total neutral oxygen is in dust. On the other hand, Gattuzz et al. (2014) suggested that the oxygen edge can be fitted only with gaseous oxygen. Later, Eckersall et al. (2017) studied the gas features in the oxygen K-edge region with the models used in Gattuzz et al. (2015). They noticed strong residuals in the fit and they mentioned that they are likely due to dust. Furthermore, Joachimi et al. (2016) searched for evidence of CO in XMM-Newton spectra of low-mass X-ray binaries and suggested two weak detections.

In the literature there are different studies regarding the atomic data in the oxygen K-edge region. Theoretical calculations on the K-shell photoabsorption of oxygen ions have been performed by García et al. (2005) and McLaughlin & Kirby (1998) using the R-matrix approach. Moreover, laboratory measurements have been carried out in order to determine the absolute energy of the photoabsorption cross sections of oxygen ions (Menzel et al. 1996, Stolte et al. 1997). Gorczyca et al. (2013) present an analytical formula to describe with accuracy the photoabsorption cross section of O I in X-ray spectral modelling and Leutenegger et al. (2020) discuss an experimental technique for the determination of the absolute calibration of the oxygen  $K_{\alpha}$  transition energy. Finally, Frati et al. (2020) review the oxygen K-edge X-ray absorption spectra of atoms, molecules and solids, where the oxygen 1s core electron is excited to the lowest empty states at  $\sim 530$  eV.

In order to determine the presence of dust in the oxygen K-edge, we need to use accurate dust models. To this end, we perform a laboratory measuring campaign to compute the absorption cross sections of 18 dust compounds with different chemical composition, such as different types of silicates and oxides. In order to investigate the crystallinity, our samples contain both crystalline and amorphous dust grains. From studies of the  $10\ \mu\text{m}$  silicate feature in the mid-IR band it has been found that the stoichiometry of silicate dust is mostly amorphous olivines ( $\text{Mg}_{2-x}\text{Fe}_x\text{SiO}_4$ ) and pyroxenes ( $\text{Mg}_{1-x}\text{Fe}_x\text{SiO}_3$ ) (Kemper et al. 2004, Min et al. 2007). Also, Kemper et al. (2004) found that towards SgrA\* most silicates have an amorphous structure and less than 2.2% are crystalline. They have also reported that  $\sim 85\%$  of the amorphous grains are olivines and  $\sim 15\%$  pyroxenes. The pyroxenes are found to be slightly Mg-rich with  $\text{Mg}/(\text{Mg}+\text{Fe}) \sim 0.55$ , while

the olivines may be Fe-rich. Min et al. (2007) conclude that the amorphous silicates are Mg-rich with  $\text{Mg}/(\text{Mg}+\text{Fe}) \sim 0.9$ . They also find that the crystallinity in the ISM is small and they report a pure crystalline forsterite grain composition ( $\text{Mg}_2\text{SiO}_4$ ). Moreover, experimental studies of astrophysical dust analogues with application to infrared observations have been presented by Nuth et al. (2002).

We apply the new dust models to the high-resolution XMM-Newton RGS spectrum of Cygnus X-2 in order to study the oxygen K-edge spectral region. It is a bright X-ray source with a moderate column density ( $\sim 2 \times 10^{21}\text{cm}^{-2}$ , Juett 2004) and high flux ( $2.3 \times 10^{-9}\text{erg/sec/cm}^2$  in the 0.3-2 keV band). Cygnus X-2 has been proposed as a Z-track source (Hasinger & van der Klis 1989) and believed to reach the Eddington luminosity limit during its high state (Bałucińska-Church et al. 2010, Mondal et al. 2018, King & Ritter 1999). The distance of the source has been estimated to be around 7 – 12 kpc and its galactic coordinates are  $l, b = 87^{\circ}.33\text{-}11^{\circ}.32$ , which means that it is located about 1.4 - 2.4 kpc away from the Galactic plane (Cowley et al. 1979, McClintock et al. 1984, Smale 1998, Yao et al. 2009). The systemic velocity of the binary system was found to be about -220 km/s (Cowley et al. 1979, Casares et al. 1998).

Previous studies of Cygnus X-2 with Chandra gratings showed that the oxygen region is possibly mildly absorbed by interstellar dust (Yao et al. 2009). Moreover, Juett (2004) studied the Chandra HETGS spectrum of Cygnus X-2 and they mentioned that features from dust or molecular compounds are not essential to obtain a good fit. The goal of this investigation is to understand the contribution of dust to the oxygen K-edge spectral region using up-to-date laboratory and atomic data measurements.

The paper is organised as follows. In Section 2 we describe the dust samples used in this work, the laboratory experiment and the treatment of the laboratory data. In Section 3 and Appendix A we present the methodology used to calculate the dust extinction cross sections for the oxygen K-edge. In Section 4 we apply the new models to the RGS spectrum of Cygnus X-2. The discussion of our results is presented in Section 5, and in Section 5.3 we compare the results obtained using both the atomic databases of SPEX and XSTAR for the O I, O II and O III lines. In Section 6 we discuss the prospects of observing the oxygen K-edge region with the Arcus concept mission. In Section 7 we present the conclusions.

## 2. The laboratory experiment

### 2.1. The dust samples

The dust samples used in this work are laboratory analogues of silicates and oxides of astronomical interest. The choice of samples reflects the astronomical silicate composition which has been discussed in previous studies (Jaeger et al. 1998, Kemper et al. 2004, Chiar & Tielens 2006, Min et al. 2007, Olofsson et al. 2009, Draine & Lee 1984). In Table 1 we present the list of the samples. The first column shows the reference number of each sample. In the second and third columns we present the compound name and its chemical formula and in the last column its form (i.e. crystalline or amorphous). We note that in this paper we use amorphous as a collective term in order to describe all non-crystalline materials. Our amorphous samples are glassy, the structure of which may still show a short-range order of atoms. However, Si-K edge spectra of our amorphous samples show a smooth profile, significantly distinct from the crystal ones (Zeegers et al. 2019).

Most of the compounds have already been presented in previous

works where the Mg, Fe, and Si K-edges have been measured in the laboratory using the Synchrotron facilities (Zeegers et al. 2017, 2019, Rogantini et al. 2018). Among the samples, four of them are natural (samples 2, 7, 9, 16 in Table 1) and six are commercial products (samples 11, 12, 13, 15, 17, 18). The rest of the silicate samples are synthesized in the laboratories at the Astrophysikalisches Institut und Universitäts-Stenwarte (AIU) and Osaka University (for details see Zeegers et al. 2019). Our list of 18 samples contain pyroxenes, olivines and oxides. The silicate samples consist of different Mg/(Mg+Fe) ratio, between 0.5 and 0.9 and can be found in both amorphous and crystalline form. We also include magnesium pure compounds such as forsterite and enstatite (sample 7, 8, 11) and the iron pure compound named fayalite (sample 10). Additionally, we have 3 different types of quartz (samples 16, 17, 18), one in crystalline form and two in different stages of amorphisation.

## 2.2. The Electron Energy Loss measurements

We perform laboratory measurements of dust in the oxygen K-edge using the STEM (Scanning Transmission Electron Microscope) facility at the University of Cadiz. Electron energy loss spectroscopy (EELS) is a technique which measures the change in the kinetic energy of electrons after the interaction with the sample. This provides structural and chemical information of the material studied. The interaction between the incident electron beam and the materials, in our case the dust samples, results in electron energy loss. A typical energy loss spectrum contains many features and is separated into three spectral regions. The so-called *zero-loss* peak represents electrons that are transmitted without suffering measurable energy loss. The *low-loss* spectrum corresponds to electrons that have interacted with the weakly bound electrons of the atoms and finally the *core-loss* region which contains the electrons that have interacted with the tightly bound core electrons (Egerton 2011). The *core-loss* region contains the information on the fine structures of dust, also referred to as Energy Loss Near Edge Structures (ELNES). Both ELNES and XAFS present exactly the same spectral shape under the dipole approximation.

For the purpose of this experiment we use the Titan Cubed Themis 60-300 microscope in the STEM mode, operating at 200 keV. In parallel, high-spatial resolution EELS experiments were performed with the spectrum-imaging mode which allows the correlation of analytical and structural information on selected regions of the studied material. In this way we compare the information of the spectra with those of the spatial distribution of the sample. These supporting information experiments were acquired in Dual EELS mode using an energy dispersion of 0.25 eV, 50 pA probe current, and 50 ms acquisition time per EELS spectrum (Manzorro et al. 2019).

The STEM mode of the Electron Microscope enables us to scan pixel by pixel the dust samples. The resulting spectrum will be the average spectrum of each pixel. To improve the signal-to-noise ratio of our data we obtain 5-10 measurements of individual selected regions of interest on the dust sample.

## 2.3. Analysing the laboratory data

In this section we describe step by step the analysis of the raw laboratory measurements. We use the *python* library *hyperspy*<sup>1</sup>

to convert the laboratory data to a python-readable format.

- *Thickness selection*: The dust samples have an intrinsic thickness variation. In the EELS, as the thickness of the area under study increases, the strong interaction of the primary electrons within the grain will result in multiple scattering events. This tends to reduce the signal-to-noise ratio of the EELS edges. To this end we need to apply a selection criterion. We select the part of the grain which belongs to thinner regions and then we consider the total spectrum of this part (see Fig. 1). In most cases, we exclude the part of the grain with  $t/\lambda > 1$ , where  $t$  is the thickness of the sample and  $\lambda$  the mean free path of the inelastic scattering.

- *Spectrum alignment*: An important correction in the EELS measurements is the alignment of the energy axis of the spectrum. For this reason we obtain the so-called *low-loss* spectrum which contains the zero loss peak (Egerton 2011). The zero loss peak is a sharp peak with an energy loss of zero appearing in an EELS spectrum. We obtain this spectrum for every measurement.

- *Background subtraction*: Next, we remove the EELS background by fitting a polynomial to the data.

- *Testing energy calibration uncertainties*: In laboratory experiments one needs to be careful about the absolute energy of the measured edges. It is possible that the calibration of the instrument is not perfect and therefore a verification of the absolute energy values has to be done. Therefore, we test the position of the oxygen edges with a reference feature that appears in our measurements. This narrow feature is a pre-peak of the oxygen edge and it is associated with an electron transition into molecular oxygen ( $O_2$ ), which is thought to evaporate due to the impact of the incident electron beam and the sample. We adopted a value of 530.5 eV for the absolute energy of the  $O_2$  transition (Jiang & Spence 2006, Garvie 2010).

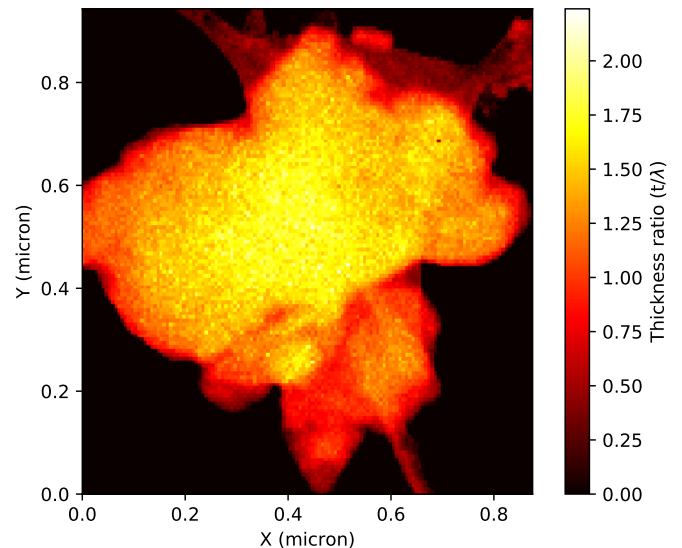


**Fig. 1.** Example of the region of interest on the dust sample obtained from laboratory data. The colourbar of the image indicates the thickness ratio  $t/\lambda$ , where  $t$  is the thickness and  $\lambda$  the mean free path of the inelastic scattering.

<sup>1</sup><https://hyperspy.org/>

**Table 1.** List of dust samples.

Sample number	Compound name	Chemical Formula	Form
1	Olivine	MgFeSiO <sub>4</sub>	amorphous
2	Olivine	Mg <sub>1.56</sub> Fe <sub>0.4</sub> Si <sub>0.91</sub> O <sub>4</sub>	crystalline
3	Pyroxene	Mg <sub>0.9</sub> Fe <sub>0.1</sub> SiO <sub>3</sub>	amorphous
4	Pyroxene	Mg <sub>0.9</sub> Fe <sub>0.1</sub> SiO <sub>3</sub>	crystalline
5	Pyroxene	Mg <sub>0.6</sub> Fe <sub>0.4</sub> SiO <sub>3</sub>	amorphous
6	Pyroxene	Mg <sub>0.6</sub> Fe <sub>0.4</sub> SiO <sub>3</sub>	crystalline
7	Enstatite	MgSiO <sub>3</sub>	crystalline
8	Enstatite	MgSiO <sub>3</sub>	amorphous
9	Hypersthene	Mg <sub>1.502</sub> Fe <sub>0.498</sub> Si <sub>2</sub> O <sub>6</sub>	crystalline
10	Fayalite	Fe <sub>2</sub> SiO <sub>4</sub>	crystalline
11	Forsterite	Mg <sub>2</sub> SiO <sub>4</sub>	crystalline
12	Spinel	MgAl <sub>2</sub> O <sub>4</sub>	crystalline
13	Corundum	Al <sub>2</sub> O <sub>3</sub>	crystalline
14	Pyroxene	Mg <sub>0.75</sub> Fe <sub>0.25</sub> SiO <sub>3</sub>	amorphous
15	Magnetite	Fe <sub>3</sub> O <sub>4</sub>	crystalline
16	Quartz	SiO <sub>2</sub>	crystalline
17	Quartz	SiO <sub>2</sub>	amorphous
18	Quartz	SiO <sub>2</sub>	amorphous

### 2.3.1. Principal Component Analysis

We perform a Principal Component Analysis (PCA) to further test if the samples are homogeneous in composition and thickness. The original idea of PCA was established by Karl Pearson in 1901 (Pearson 1901). The PCA is a statistical procedure that uses an orthogonal transformation to find inhomogeneity in a set of data. It decomposes a dataset into a set of orthogonal eigenvectors or principal components. When the PCA is applied to a set of spectra, the result is a set of spectral components which describe the variability of the data. The first principal component is the eigenvector that corresponds to the data with the maximum variation. The second eigenvector will show the second highest variation of the data and it is orthogonal to the first one. Every principal component will reveal the characteristic features of the spectrum in order of variation.

The dust grains may present inhomogeneities. Using the PCA, we cross check if the selected area on the grain is homogeneous. If it is not homogeneous we repeat the analysis for this specific measurement. This procedure is useful in order to obtain robust results and avoid artifacts in the spectra.

### 3. From laboratory measurements to cross sections

From the EELS experiment we obtain the information about the fine structure of dust for each sample. Next, we need to calculate the extinction cross section in order to adopt the laboratory measurements for astronomical data analysis. The methodology used by us has been described extensively in previous works of Zeegers et al. (2017) and Rogantini et al. (2018). Here, we discuss the main steps of this analysis, adjusted for the oxygen K-edge.

When the X-ray light pass through a material, it can be either transmitted, absorbed, or scattered. The transmittance of a mate-

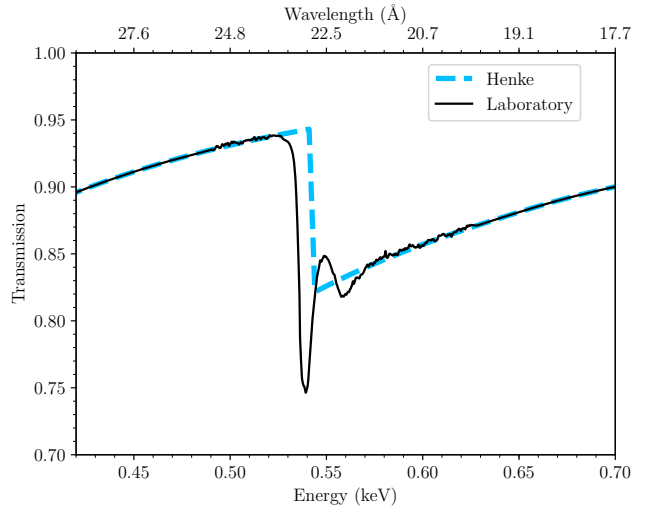


**Fig. 2.** Transmission spectrum in the oxygen K-edge using of amorphous olivine dust compound (black solid line). The blue dashed line indicates the tabulated data found in Henke et al. (1993), which were used to fit the pre-edge and post-edge of the data.

rial is the amount of light that is transmitted and it is described by the Beer-Lambert law:

$$T = \frac{I}{I_0} = e^{-\mu \cdot x}$$

where  $I$  is the transmitted and  $I_0$  the incident light intensity. In the above equation  $\mu$  is the attenuation coefficient in  $\mu\text{m}^{-1}$  which depends on the properties of the material and  $x$  describes the depth of the radiation in the material, i.e. the thickness of the



sample (in  $\mu\text{m}$ ). The thickness should be 2-3 times below the attenuation length to avoid the thickness effects which can reduce the XAFS amplitude (Parratt et al. 1957, Bunker 2010). For the attenuation length we use the tabulated values obtained from the Center for X-Ray Optics at Lawrence Berkeley National Laboratory (CXRO)<sup>2</sup>. In this work, we choose a thickness of  $0.05 \mu\text{m}$  for all our samples, a necessary value in order to calculate the optical constants. This is consistent with the mean value of the EELS thickness of our samples which varies from  $\sim 0.01 \mu\text{m}$  to  $\sim 0.09 \mu\text{m}$ .

In Figure 2 we present the transmittance of an olivine compound obtained using the EELS. The pre-edge ( $< 0.525 \text{ keV}$ ) and the post-edge ( $> 0.575 \text{ keV}$ ) have been fitted to the tabulated values from CXRO (Henke et al. 1993).

### 3.1. Optical constants

In order to calculate the total extinction cross section of our samples we need to determine first the optical constants of the complex refractive index which is defined as:

$$m = n + ik$$

The refractive index is a complex number that describes how the light propagates into a material. The real part shows the dispersive behavior on the incident light and the imaginary part its absorption. In the literature there are different notations to describe the optical constants (Rogantini et al. 2018).

The imaginary part ( $k$ ) can be calculated directly from the data and the thickness of each sample from the equations:

$$k = \frac{\mu\lambda}{4\pi} \quad \mu = -\frac{\ln T}{x}$$

where  $\lambda$ , represents the wavelength of the incident X-ray and  $T$  the transmittance. Knowing the imaginary part of the refractive index, we use the Kramers-Kronig relations to calculate the real part. The Kramers-Kronig relations are mathematical relations that connect the real and imaginary parts of any complex function. These relations are used to calculate the real part from the imaginary part (or vice versa) of functions in physical systems. Here, to calculate the real part we use the python package *kkcalc*<sup>3</sup>. This tool uses the optical constants in terms of atomic scattering factors,  $f_1$  and  $f_2$  which are described in Watts 2014 (see also Rogantini et al. 2018). In Figure 3 we present the optical constants for the amorphous olivine (compound # 1).

### 3.2. Total extinction cross section

When the optical constants  $n$  and  $k$  have been calculated, one can proceed to the calculation of the total extinction cross section. To calculate the extinction cross section we apply the Mie theory (Mie 1908). Therefore, we use the python module *miepython*<sup>4</sup> which is the python version of MIEV0 code described in Wiscombe (1980).

The Mie code calculates the extinction and scattering efficiency factors ( $Q$ ). Then, the scattering, extinction and absorption cross sections are calculated from the efficiency factors of each grain of radius  $r$  ( $C = \pi r^2 Q$ ). However, the interstellar dust grains can

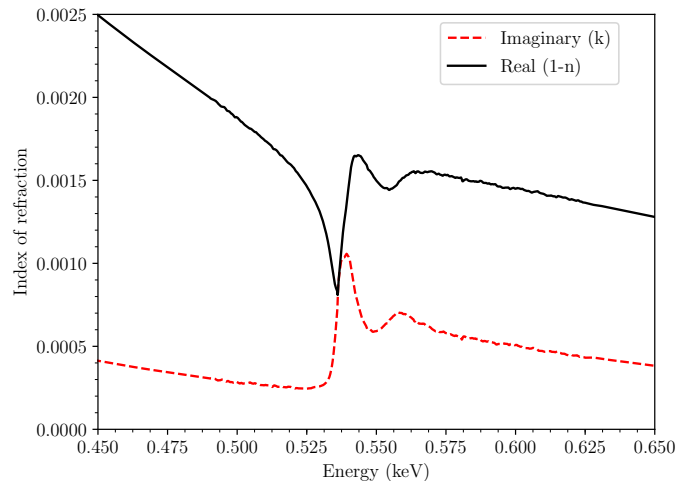


**Fig. 3.** Real and imaginary part of the refractive index calculated using the Kramers-Kronig relations for the amorphous olivine.

be found in different sizes in the interstellar medium. To obtain the total scattering, extinction and absorption cross sections one needs to integrate over a grain size distribution:

$$\sigma(\lambda) = \int_{a_-}^{a_+} Q \cdot n(r) dr$$

where  $n(r)$  is the size distribution. We use the Mathis-Rumpl-Nordsieck model (MRN, Mathis et al. 1977):

$$n(r)dr = A_i n_H r^{-3.5} dr$$

where  $n_H$  is the number density of H atoms and  $A_i$  is a normalisation constant which depends on the type of dust. The normalisation constant is calculated using the equations described in Mauche & Gorenstein (1986), and Hoffman & Draine (2016). For the purpose of this paper, we calculate the extinction cross section to be implemented into the *amol* model of the software package SPEctral X-ray and UV modelling and analysis, SPEX, version 3.05.00<sup>5</sup> (Kaastra et al. 1996; Kaastra et al. 2018).

In Fig. 4 we present the calculated extinction, absorption and scattering cross sections for amorphous olivine. In Appendix A we present the extinction cross sections for all compounds used in this work. The oxygen compounds measured in the laboratory show a smooth absorption profile. Contrary to the Si K-edge (Zeegers et al. 2019) the differences among the different types of silicates are negligible. However, we note a difference between the amorphous and crystalline structure of the same compound. This effect is due to the different configuration of the atoms in the grain.

## 4. Application to the astronomical data

X-ray spectra of X-ray binaries can be used to study the interstellar medium in several lines of sight in the Galaxy through the absorption features of dust and gas. Thus, we implement the laboratory data into a complete spectral model and apply

<sup>2</sup><http://www.cxro.lbl.gov/>

<sup>3</sup><https://pypi.org/project/kkcalc/>

<sup>4</sup><https://github.com/scottprahl/miepython>

<sup>5</sup><http://doi.org/10.5281/zenodo.2419563>

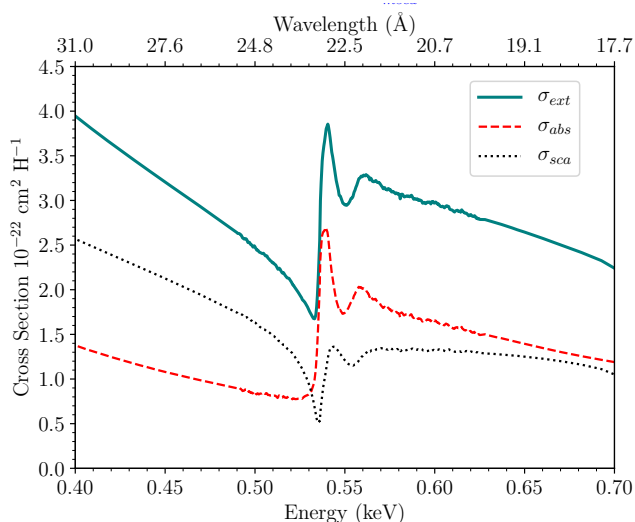


**Fig. 4.** Calculated extinction ( $\sigma_{\text{ext}}$ ), absorption ( $\sigma_{\text{abs}}$ ) and scattering ( $\sigma_{\text{sca}}$ ) cross section of dust per hydrogen nucleus. The figure shows the amorphous olivine composition in the oxygen K-edge region.

them to Cygnus X-2, an ideal X-ray target to study the composition of the interstellar oxygen. For this analysis we use data from the Reflection Grating Spectrometer (RGS) on board the XMM-Newton satellite (den Herder et al. 2001). The RGS has a resolving power of  $R = \frac{\lambda}{\Delta\lambda} \gtrsim 400$  and an effective area of  $\sim 45 \text{ cm}^2$  around the oxygen K-edge.

#### 4.1. Data reduction

We reduce the XMM-Newton data using the Science Analysis Software, SAS (ver.16). First, we run the *rgsproc* command to create the event lists. Then, we filter the RGS event lists for flaring particle background using the default value of 0.2 counts/sec threshold. We also exclude the bad pixels using *keepcool=no* in the SAS task *rgsproc*. We use in total 4 long observations, listed in Table 2. In bright sources, some areas of the grating data may be affected by pile-up. In order to recognise the spectral regions not affected by pile-up one can compare the first and the second order for each grating (Costantini et al. 2012). We have negligible pile up in all the observations used in this paper. The spectral shape does not significantly vary through different epochs and this allows us to combine the data using the SAS command *rgscombine* in order to obtain a higher signal-to-noise ratio.

**Table 2.** XMM-Newton observation log

Obs. ID	Obs. Date	Exp. Time (ks)
0303280101	14-06-2005	32
0111360101	03-06-2002	22
0561180501	13-05-2009	24
0602310101	12-05-2009	86

**Notes.** The exposure time refers to the net value, before the background filtering. The filtering causes the total exposure (sum of all the observations) to be reduced by  $\sim 40$  ks.

#### 4.2. Spectral fitting

In Figure 5 we present the stacked RGS spectrum of Cygnus X-2. The spectrum displays narrow absorption features near the oxygen ( $\sim 23 \text{ Å}$ ), neon ( $\sim 13.5 \text{ Å}$ ), and iron ( $\sim 17.5 \text{ Å}$ ) edges, which are produced by ionised gas in the ISM. In this work we mainly focus on the neutral and mildly ionised gas. We fit the spectrum in the range of 10–35 Å using SPEX. To evaluate the goodness of our fit we adopt  $C$ -Statistics which is denoted as  $C_{\text{stat}}$  in the rest of the manuscript. SPEX uses  $C_{\text{stat}}$  as described in Cash (1979) but with an addition which allows an estimate of the goodness of the fit (for details see Kaastra 2017). Also, in our analysis we use the proto-Solar abundance units of Lodders & Palme (2009).

The continuum emission of low-mass X-ray binaries originates from their accretion disk and corona, and may be described as a blackbody and a Comptonised emission component, respectively (see Done et al. 2007). As RGS provides a relatively narrow energy band, the full shape of the spectral energy distribution cannot be constrained. Thus, we use a simple power law model (*pow* in SPEX), which reproduces well the continuum shape in the RGS band.

##### 4.2.1. The gas phase modelling

We further adopt a neutral gas component (*hot* model in SPEX) to absorb the continuum. The *hot* model calculates the transmission of a plasma in collisional ionisation equilibrium (de Plaa et al. 2004). For a given temperature and set of abundances, the model calculates the ionisation balance and then determines all the ionic column densities by scaling to the prescribed total hydrogen column density. At low temperatures ( $\sim 0.5 \text{ eV}$ ) the *hot* model is effectively representing the neutral gas, since this temperature is sufficiently low to obtain neutral species. In this model both the hydrogen column density and the temperature (eV) are free parameters. This provides a physical fit of the ISM because we can distinguish between the different temperature phases along this line of sight.

We need in total three *hot* components to fit the weakly and mildly ionised features. These correspond to three different ISM temperatures along this line of sight: a quasi-neutral gas component with  $kT \sim 0.7 \text{ eV}$ , a warmer component with  $kT \sim 2.5 \text{ eV}$  and a hotter one with  $kT \sim 12 \text{ eV}$  (Fig 6). The parameters of the fit are shown in Table 3. We limit the temperature range of the cold gas to a maximum of 0.7 eV in order to have the cold gas phase dominated by neutral oxygen.

The stacked spectrum of Cygnus X-2 presents additional features: some absorption-like features around 24–25 Å and a ‘bump’ around 24–26 Å. The strongest absorption-like features are at 24.7 Å and at 24.3 Å and their positions do not correspond to lines from known ions. In fact, they correspond to absorption features in the effective area of RGS. We concluded that these dips are most likely due to calibration issues associated to bad pixels and therefore can be ignored.

Moreover, the ‘bump’ in the continuum around 24–26 Å is too narrow to be associated with any continuum components. A similar bump is also observed after the Fe L-edge (around 18 Å). These excesses have been associated to broad line emission features (Madej et al. 2010, 2014). For the improvement of our modelling we fit this excess with Gaussian profiles in order to prevent residuals in the oxygen edge region from a badly-fitted continuum and uncertainties in the determination of the absorp-

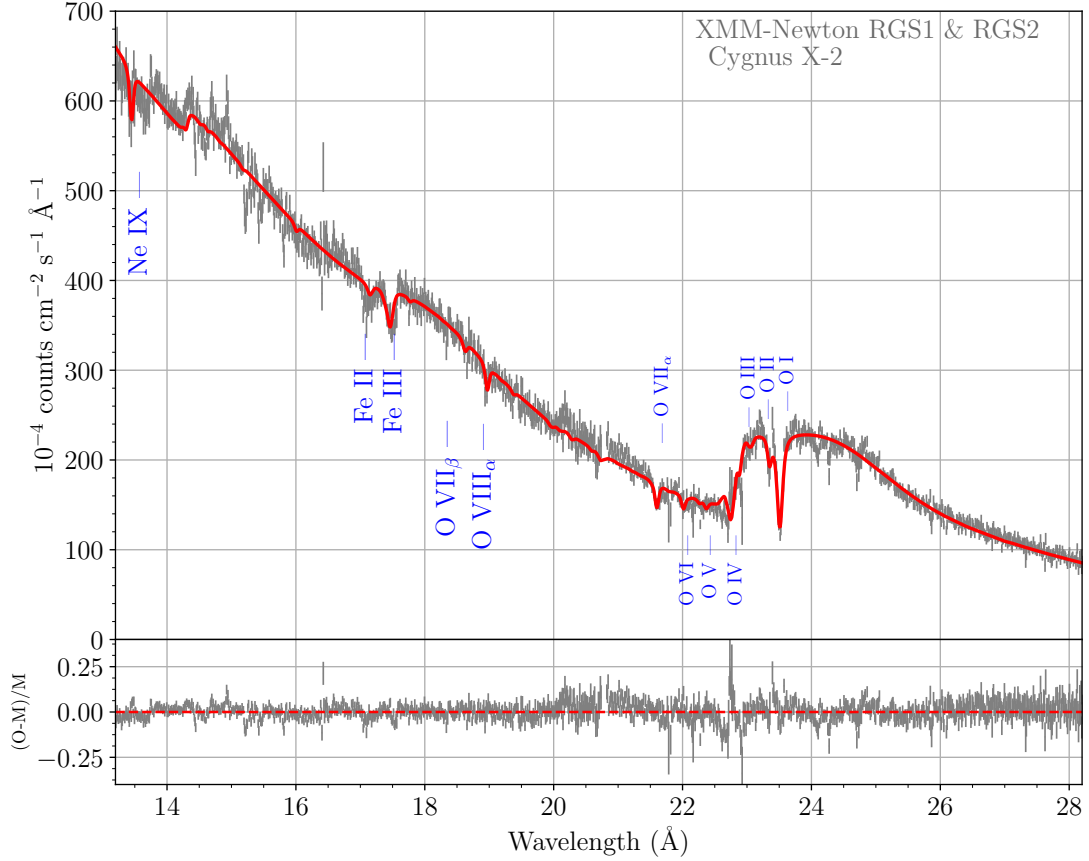


**Fig. 5.** Top panel: XMM-Newton RGS spectrum of the low-mass X-ray binary Cygnus X-2 and the best fit model. Lower panel: Residuals of the best fit model, where  $(O-M)/M$  is  $(\text{Observed-Model})/\text{Model}$ .

**Table 3.** Best fit parameters for Cygnus X-2.

Component	Parameter	Value
pow	norm	$88.4 \pm 0.5$
	$\Gamma$	$1.25 \pm 0.01$
hot # 1	$N_H$	$1.9 \pm 0.1$
	$kT$	$0.7 \text{ (fixed)}$
hot # 2	$N_H$	$0.05 \pm 0.01$
	$kT$	$2.5 \pm 0.9$
hot # 3	$N_H$	$0.05 \pm 0.01$
	$kT$	$11.7 \pm 0.4$

**Notes.** The symbol  $kT$  represents the temperature in eV and the  $N_H$  is the column density in  $10^{21} \text{ cm}^{-2}$ . The symbol  $\Gamma$  is the photon index and the normalisation of the power law is in units of  $10^{44} \text{ ph/s/keV}$  at 1keV.

tion parameters. Thus, we leave the interpretation on the nature of these ‘bumps’ open.

#### 4.2.2. The oxygen edge region

Here, we focus our analysis in the oxygen edge spectral region (19 – 26 Å) which displays several sharp absorption features. We follow a similar fitting procedure for the oxygen edge as in Costantini et al. (2012). The best fit is shown in the top panel of Figure 6 and in the lower panel we present the contribution of each absorption component. The 0.7 eV gas (see Section 4.2.1)

**Table 4.** Best fit parameters of the slab component. The symbol  $N_{\text{ion}}$  represents the ionic column density.

ion	$\log N_{\text{ion}} \text{ (cm}^{-2}\text{)}$
O VI	$15.4 \pm 0.1$
O VII	$15.9 \pm 0.1$
O VIII	$15.8 \pm 0.1$

imprints the line from O I at 23.5 Å and is mimicing the neutral gas. At this stage, from our fit we obtain  $C_{\text{stat}} = 1702$  for 786 degrees of freedom ( $d.o.f.$ ). At shorter wavelengths, the gas component with higher temperature of  $kT = 2.5 \text{ eV}$  produces the absorption by O II (23.36 Å). A third component with slightly smaller contribution to the total fit takes into account the O III absorption line together with some weaker O IV and O V lines. At wavelengths 22 Å, 21.6 Å, 18.9 Å the lines of O VI, O VII and O VIII respectively, are the signature of an even hotter phase of the ISM. We take into account absorption by this hot gas using the slab model in SPEX. This model calculates absorption by a slab of optically-thin gas, where the column density of ions are fitted individually and are independent of each other (see Table 4). The additional hot models and the slab model improve our fit and we obtain  $C_{\text{stat}/d.o.f.} = 1380/772$ .

Finally, we test the effect of our new calculated dust extinction cross sections implemented into the amo1 model of SPEX. We let the column density of the amo1 model free to vary as well as

the depletion of the hot model (hot # 1, cold phase) of oxygen and iron. The depletion of silicon is fixed to 90% according to the literature (Rogantini et al. 2019, Zeegers et al. 2019) and the depletion of magnesium is constrained to be at least 80%.

In Figure 6 we present the best fit using an olivine dust compound (amorphous olivine, compound # 1 in Table 1). In the lower panel of Figure 6 we present the transmission of the dust component (in magenta). As shown, the transmission of the dust covers a broad area of the oxygen K-edge spectral region from about 22.3 Å to 22.5 Å. By adding the dust model we obtain  $C_{\text{stat}}/d.o.f. = 1342/771$ .

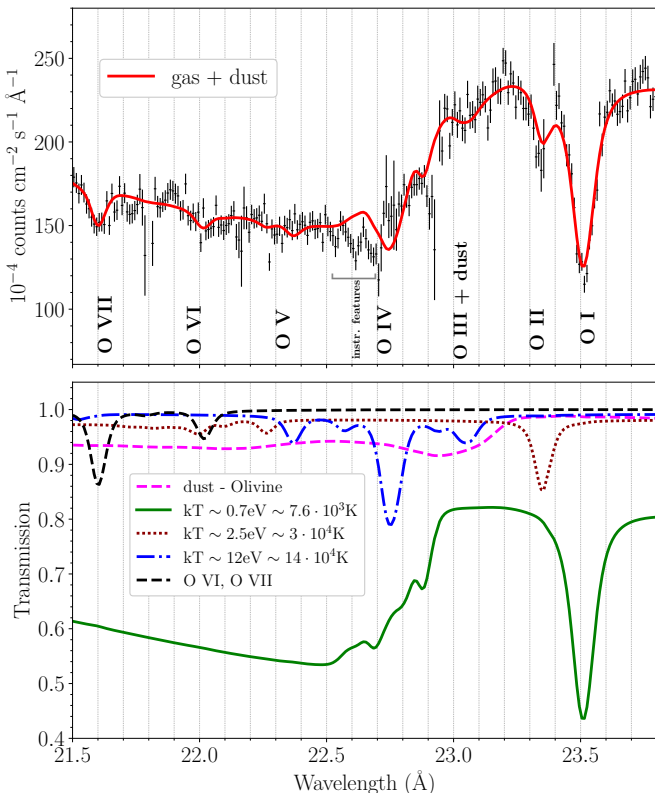


**Fig. 6.** Top panel: XMM-Newton RGS spectrum of the low-mass X-ray binary Cygnus X-2. Best fit around the oxygen K-edge. Lower panel: The transmission of each component. The transmission of the colder component of the ISM has been multiplied by a factor of 2.5 for display purposes.

#### 4.3. The dust modelling

Our fit takes into account the contribution of dust using the newly calculated extinction models. The analysis above has been carried out using an amorphous (glassy) olivine composition ( $\text{MgFeSiO}_4$ ). However, the ISM consists of a mixture of chemical elements. We have further tested different combinations of dust compounds from the list in Table 1, containing silicates and oxides, to search for the best fit combination which describes the interstellar dust composition in the oxygen edge. The amol model in SPEX allows us to test 4 different compounds at a time. The number of different combinations is given by the equation:

$$C_{e,c} = \frac{e!}{c!(e-c)!}$$

where  $e$  is the number of the available edge profiles and  $c$  the combination class (see also Costantini et al. 2012). In our fit we do not include the aluminium compounds (Table 1, compounds # 12 and 13) since this element is outside the RGS energy band and it is believed that they exist in small quantities in the ISM. We fit with the remaining 16 compounds which gives 1820 different combinations.

To compare the different models we use a robust statistical approach. The standard model comparison tests (such as the  $\chi^2$  Goodness-of-Fit test) cannot be used because our models are not nested (Protassov et al. 2002). Therefore, we perform the Akaike Information Criterion (AIC) which represents a robust and fast way to select the models which have more support from the data (Akaike 1974), as explained in detail in Rogantini et al. (2019). AIC gives the relative quality of statistical models for a given set of data.

We calculate the AIC difference ( $\Delta AIC$ ) over all candidate models with respect to the model which has the lowest AIC value. The most significant model is the one which minimises the AIC value. Using the criteria of Burnham & Anderson (2002), the models with  $\Delta AIC > 10$  can be ruled out. From the total of 1820 models we obtain using the different combinations, about 590 of them were found with  $\Delta AIC > 10$  and are therefore excluded. These models contain mostly Quartz (compounds # 16, 17, 18 in Table 1). The rest of the models, with  $\Delta AIC < 10$ , are plausible to represent the data. In particular, models with  $\Delta AIC < 2$  can fit equally well the oxygen edge. We obtain 311 different models with  $\Delta AIC < 2$ . We conclude that we do not have sufficient resolution to distinguish between the different dust samples. The modelling is further complicated by the relative similarity of the oxygen absorption dust profiles measured in the laboratory (Appendix A).

## 5. Discussion

### 5.1. The multi-phase gas in the ISM

The study of the ISM through the X-ray absorption features of bright background sources, such as X-ray binaries, is a unique tool to probe the different phases of the ISM. By studying the oxygen K-edge spectral region, we can constrain different gas temperatures by probing low and high ionisation gas, covering from O I to O VII. With our modelling, we find a column density of oxygen in the gas phase of  $\sim 1.27 \times 10^{18} \text{cm}^{-2}$  which corresponds to  $(93 \pm 9)\%$  of the total column density. The remaining  $(7 \pm 1)\%$  corresponds to solid phase (dust) with column density of  $\sim 9 \times 10^{16} \text{cm}^{-2}$ . Considering the errors, if the percentage is lower or higher than 100% this implies that there is under or over abundance of oxygen, relative to the assumed abundances.

In our modelling the gas consists of 3 components (see Table 3). We have a cold gas component with temperature  $kT = 0.7 \text{ eV}$  (or  $T \sim 8 \times 10^3 \text{ K}$ ), a warm component with  $kT = 2.5 \text{ eV}$  (or  $T \sim 3 \times 10^4 \text{ K}$ ) and finally a hot component with  $kT = 12 \text{ eV}$  (or  $T \sim 14 \times 10^4 \text{ K}$ ).

In Table 5 we present the column density of each oxygen ion and its contribution to the total column density. The cold component produces mainly O I, some of which is locked into dust. The warm component produces the low ionisation absorption line (O II) and the hotter component produces the O III, O IV and O V. The higher ionisation lines are reproduced using a slab



**Table 5.** Contributions to the total oxygen column density.

Phase	Constituent	$N_{\text{O}}(10^{18}\text{cm}^{-2})$	$\%N_{\text{O}}^{\text{gas}}$	$\%N_{\text{O}}^{\text{total}}$
Gas	O I	$1.2 \pm 0.1$	$95 \pm 9$	$93 \pm 9$
	O II - O IV	$0.05 \pm 0.01$	$4.0 \pm 0.8$	
	O VI - O VIII	$0.020 \pm 0.001$	$1.00 \pm 0.01$	
Dust	Silicates	$0.09 \pm 0.01$		$7 \pm 1$

**Notes.**  $N_{\text{O}}$  represents the total column density,  $\%N_{\text{O}}^{\text{gas}}$  is the contribution of each gas constituent to the respective phase and  $\%N_{\text{O}}^{\text{total}}$  is the contribution of the different phases to the total column density.

**Table 6.** Oxygen column densities and abundances.

$N_{\text{gas}}$	$(1.27 \pm 0.09) \times 10^{18}\text{cm}^{-2}$
$N_{\text{dust}}$	$(0.09 \pm 0.01) \times 10^{18}\text{cm}^{-2}$
$A_{\text{gas}}$	$(6.1 \pm 0.6) \times 10^{-4}$
$A_{\text{dust}}$	$(0.45 \pm 0.07) \times 10^{-4}$
$A/A_{\odot}$	$1.1 \pm 0.1$

**Notes.**  $N_{\text{gas}}$  and  $N_{\text{dust}}$  indicate the total column density of gas and dust respectively.  $A_{\text{gas}}$  and  $A_{\text{dust}}$  are the abundances of oxygen in gas and dust respectively (with respect to hydrogen).  $A/A_{\odot}$  is the total abundance (gas+dust) ratio in proto-Solar abundance units.

model in SPEX.

Molecules such as carbon monoxide are expected to be found in the ISM, especially in molecular clouds. It has been proposed that the missing oxygen from the gas phase of the ISM could be locked up in molecules together with elements with a high cosmic abundance such as CO (Jenkins 2009). To test the presence of carbon monoxide we use the cross section (Barrus et al. 1979) implemented into the amo1 model in SPEX. According to this model, such a feature is expected to be present around 23.2 Å. We obtain an upper limit of  $N_{\text{CO}} < 3.2 \times 10^{16}\text{cm}^{-2}$  which corresponds to less than 2% of the total oxygen.

### 5.2. Abundances and depletions

From the best fit of Cygnus X-2 we find a column density of neutral hydrogen of  $N_{\text{H}} = (1.9 \pm 0.1) \times 10^{21}\text{cm}^{-2}$ . This is in agreement with the hydrogen column density along this line of sight (HI4PI Collaboration et al. 2016). We find that  $(7 \pm 1)\%$  of the oxygen is depleted into dust. Pinto et al. (2010) studied the interstellar medium along the line of sight of GS 1826-238 and found that  $(10 \pm 2)\%$  of oxygen is contained within solids, such as silicates and water ice. Later, Costantini et al. (2012) studied the absorbed spectrum of 4U 1820-30 and found  $(20 \pm 2)\%$  depletion. Our best fit indicates that the amount of oxygen in gas and dust is consistent with Solar composition. The results on the abundances and depletions are presented in Table 6.

### 5.3. Comparison between the atomic databases for oxygen

Accurate high-resolution X-ray spectroscopy and interpretation require state-of-art atomic databases. The oxygen K-edge region is one of the most important and complicated astrophysical spectral regions. The available atomic X-ray databases for atomic oxygen are based on different cross section calculations. Here, we compare the photoabsorption cross sections implemented into SPEX (Kaastra et al. 1996) and XSTAR (Kallman & Bautista 2001) for the atomic oxygen O I, O II and O III. We

further examine the effect of the different atomic databases in our fitting of the oxygen edge region of the interstellar medium. Regarding XSTAR, the O I photoabsorption cross section can be found in Gorczyca et al. (2013) and for O II, O III it uses the R-matrix calculations from García et al. (2005).

For the inner K-shell transitions of oxygen ions SPEX uses the calculations provided by E. Behar (HULLAC calculations). For O I and O II the lines are shifted in order to match the Juett (2004) observational values (see Kaastra et al. 2010). Moreover, the oscillator strengths and transition rates for all O I lines have been updated with values computed by Ton Raassen using Cowan's code (Cowan 1981, T. Raassen private communication). In Appendix B we present the wavelengths and oscillator strengths of the oxygen lines implemented in SPEX.

In Figure 7 we present the comparison between the different atomic databases in the oxygen K-edge region. The top panel shows the model calculations for the atomic transitions of O I. The cross sections of O I agree with each other regarding the wavelengths of the lines. The middle panel of Figure 7 refers to O II and the bottom panel to O III. For O II and O III the absolute energy of the lines between SPEX and XSTAR is in disagreement.

We further test how the discrepancy between the atomic databases can affect the spectral fitting of Cygnus X-2. We substitute the atomic lines of SPEX for O I, O II and O III with those of XSTAR. This enables us to fit the lines of these three ions with the XSTAR atomic data. In order to do that we use the musr model which allows external models into SPEX. We fit the stacked spectrum of Cygnus X-2 using the lines for O I, O II, O III from the musr model. We keep the same modelling as described in Section 4.2.1, as well as the slab and the amo1 model. The free parameter of the musr model in our case is the column density and is fitted independently for each individual O I, O II and O III ion. We keep the ratio of the column density of these three ions consistent with the ratio of the column densities and temperatures in the hot model in SPEX in order to set a physical fit. In Figure 8 we present the best fit results. The XSTAR database gives a better fit around 22.7 Å. We have noticed that there is a weaker transition of O I in that region and using the XSTAR database we obtain reduced residuals. In the rest of the spectrum we achieve a similar fit.

## 6. Prospects of the oxygen K-edge study with the Arcus-concept mission

Future missions may provide us with suitable instruments to study the ISM in the soft X-rays ( $<1$  keV). For example the Arcus-concept mission (Smith 2016) will provide higher resolution data with a resolving power of  $R \sim 3000$ .

We perform an Arcus simulation in order to understand if we can put better constraints on the properties of the ISM and distinguish between the gas and solid phase. We use the

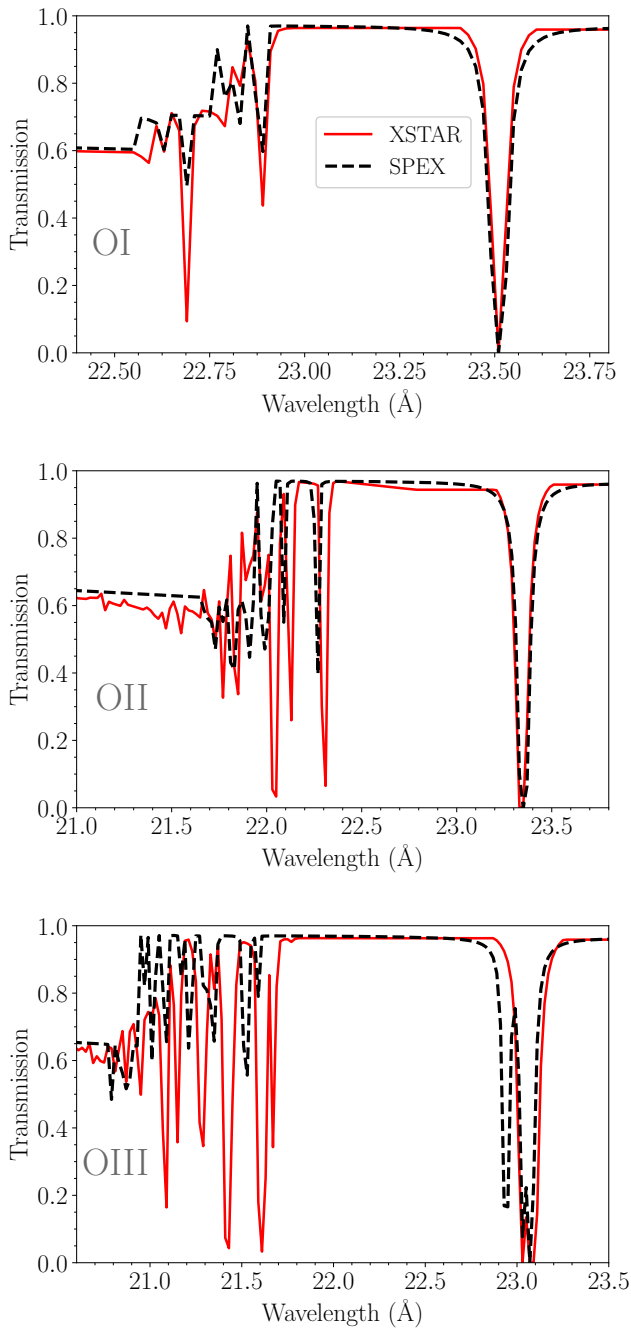


**Fig. 7.** Comparison of the atomic databases of SPEX and XSTAR at the oxygen K-edge for O I (top panel), O II (middle panel), and O III (bottom panel).

XMM-Newton RGS best fit model in the oxygen edge region described in Section 4.2.2 as a template to simulate an Arcus spectrum of Cygnus X-2. This model contains both gas and dust. In Figure 9, we present the Arcus simulation with an exposure time of 200 ks.

We test the effects of including or excluding dust in our spectrum by fitting an only-gas model (red line). It is clear from the shape of the model around 23.2 Å that with Arcus we will better distinguish the effect of dust in the oxygen K-edge. Also, the wealth of individually resolved lines will place stronger constraints on the exact structure of the multiphase gas. In general, new X-ray missions such as ATHENA and XRISM and

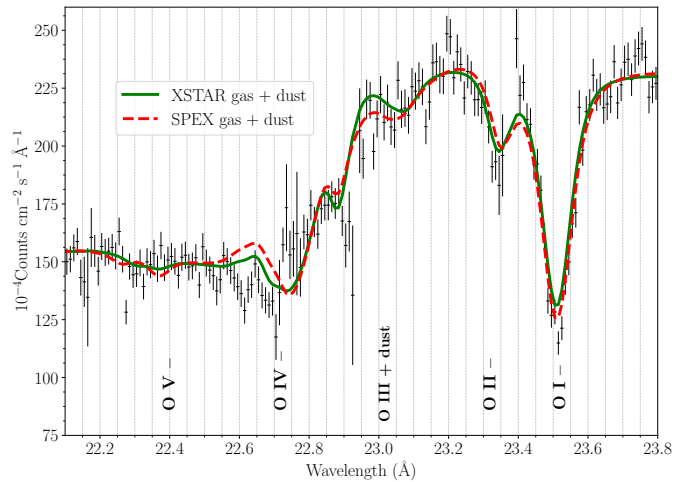


**Fig. 8.** Fitting the oxygen K-edge region using different atomic databases for the oxygen (O I, O II, O III). The plot compares the fits using the XSTAR and SPEX atomic databases. The dust compound used here is the amorphous olivine.

concept missions such as ARCUS will open up new frontiers to understand better the physics of the ISM (e.g. Rogantini et al. 2018, Costantini et al. 2019, Corrales et al. 2019).

## 7. Conclusions

In this work we present a set of laboratory measurements in the O K edge region, and we aim to characterise the absorption properties of silicates and oxides, likely forming the interstellar dust content. We have measured 18 different dust species including silicates and oxides and we have calculated the dust extinction cross sections. We adopt the laboratory data for astronomical data analysis and in particular we implemented the dust models into the SPEX X-ray fitting package. We further model the XMM-Newton RGS spectrum of Cygnus X-2 using the existing models of gas in SPEX and the new laboratory data. We focus our analysis in the oxygen K-edge region in order to study the dust and the properties of the multi-phase ISM along the line of sight to the source. We further discuss the effect of using different atomic databases for the atomic oxygen and finally we comment about new frontiers in the oxygen K-edge from the future concept mission of Arcus. Our main results are the following:

- From the oxygen K-edge we are able to study the multi-phase gas. We probe different gas temperatures and disentangle lower and higher ionised gas components, such as O I and O VIII.
- The absorption spectrum of Cygnus X-2 shows the presence of gas and dust in the oxygen K-edge region. We find that  $(93 \pm 9)\%$  of the total amount of oxygen is in the gas phase while a smaller amount of  $(7 \pm 1)\%$  is found in dust.
- The oxygen abundance along the line of sight of Cygnus X-2 is consistent with proto-Solar values. This could be due to the fact that Cygnus X-2 is located further from the Galactic center compared to other X-ray binaries.
- To fully study the dust in the oxygen K-edge we need instruments with higher resolution and effective area such as the

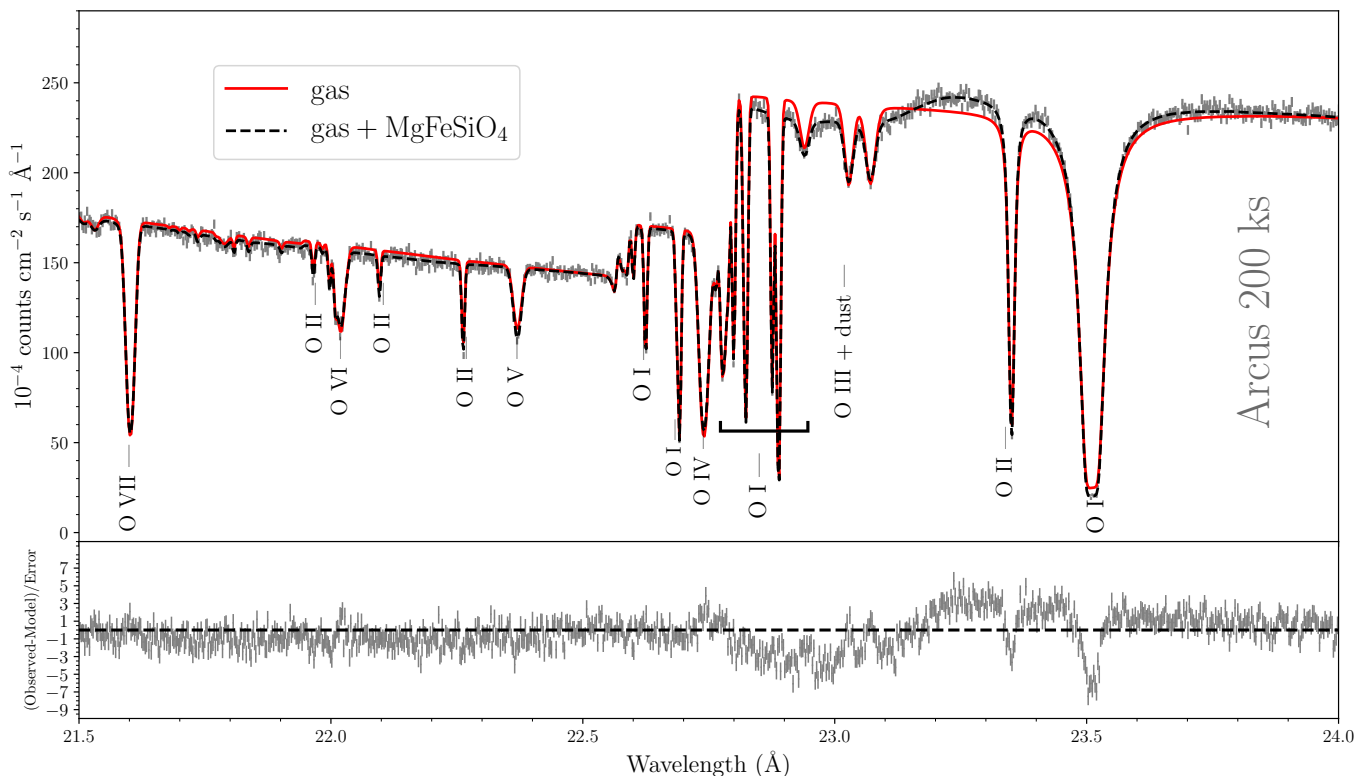


**Fig. 9.** Simulated data of Cygnus X-2 in the oxygen K-edge using the Arcus response matrix. Top panel: Simulated spectrum according to our best fit model (4.2.2) which includes dust (black dashed line). The red solid line shows the Arcus simulation without including a dust model. Bottom panel: Residuals of the fit with the gas-only model.

Arcus-concept mission. This will help to minimize the statistical noise and to better distinguish between the gas and solid phase.

- Accurate atomic databases are necessary in order to accurately study the oxygen region. The importance of the atomic data is highlighted in view of future X-ray missions.

**Acknowledgements.** We would like to thank our referee J. Nuth for the useful suggestions. IP, MM, DR and EC are supported by the Netherlands Organisation for Scientific Research (NWO) through The Innovational Research Incentives Scheme Vidi grant 639.042.525. The Space Research Organization of the Netherlands is supported financially by the NWO. The authors would like to thank E. Gattuzi for providing the cross section calculations of the atomic oxygen implemented into XSTAR, J. Garcia for valuable suggestions on atomic data and J. Wilms, R. Smith for useful information about Arcus. We thank J. de Plaa for helping with the musr model in SPEX and J. Kaastra for general instructions regarding SPEX. We also thank M. Diaz Trigo for useful information regarding Cygnus X-2.

## References

- Akaike, H. 1974, *IEEE Transactions on Automatic Control*, 19, 716
- Balucińska-Church, M., Gibiec, A., Jackson, N. K., & Church, M. J. 2010, *A&A*, 512, A9
- Barrus, D. M., Blake, R. L., Burek, A. J., Chambers, K. C., & Pregonzer, A. L. 1979, *Phys. Rev. A*, 20, 1045
- Bunker, G. 2010, Cambridge U.K., Cambridge University press
- Burnham, K. P. & Anderson, D. R. 2002, Springer
- Casares, J., Charles, P., & Kuulkers, E. 1998, *ApJ*, 493, L39
- Cash, W. 1979, *ApJ*, 228, 939
- Chiar, J. E. & Tielens, A. G. G. M. 2006, *ApJ*, 637, 774
- Corrales, L., Valencic, L., Costantini, E., et al. 2019, *BAAS*, 51, 264
- Corrales, L. R., García, J., Wilms, J., & Baganoff, F. 2016, *MNRAS*, 458, 1345
- Costantini, E., Pinto, C., Kaastra, J. S., et al. 2012, *A&A*, 539, A32
- Costantini, E., Zeegers, S. T., Rogantini, D., et al. 2019, *A&A*, 629, A78
- Cowan, R. 1981, *The Theory of Atomic Structure and Spectra*, Los Alamos Series in Basic and Applied Sciences (University of California Press)
- Cowley, A. P., Crampton, D., & Hutchings, J. B. 1979, *ApJ*, 231, 539
- de Plaa, J., Kaastra, J. S., Tamura, T., et al. 2004, *A&A*, 423, 49
- de Vries, C. P. & Costantini, E. 2009, *A&A*, 497, 393
- den Herder, J. W., Brinkman, A. C., Kahn, S. M., et al. 2001, *A&A*, 365, L7
- Done, C., Gierliński, M., & Kubota, A. 2007, *A&A Rev.*, 15, 1
- Draine, B. T. & Lee, H. M. 1984, *ApJ*, 285, 89
- Draine, B. T. & Li, A. 2001, *ApJ*, 551, 807
- Dwek, E., Zubko, V., Arendt, R. G., & Smith, R. K. 2004, in *Astronomical Society of the Pacific Conference Series*, Vol. 309, *Astrophysics of Dust*, ed. A. N. Witt, G. C. Clayton, & B. T. Draine, 499
- Eckersall, A. J., Vaughan, S., & Wynn, G. A. 2017, *MNRAS*, 471, 1468
- Egerton, R. 2011, Springer, Boston, MA, 3rd Edition
- Eiroa, C. & Hodapp, K. W. 1989, *A&A*, 210, 345
- Fraai, F., Hunault, M. O. J. Y., & de Groot, F. M. F. 2020, *Chemical Reviews* [<https://doi.org/10.1021/acs.chemrev.9b00439>], PMID: 32275144
- Gail, H. P., Zhukovska, S. V., Hoppe, P., & Tieloff, M. 2009, *ApJ*, 698, 1136
- García, J., Mendoza, C., Bautista, M. A., et al. 2005, *ApJS*, 158, 68
- Garvie, L. 2010, *American Mineralogist - AMER MINERAL*, 95, 92
- Gattuzi, E., García, J., Kallman, T. R., Mendoza, C., & Gorczyca, T. W. 2015, *ApJ*, 800, 29
- Gattuzi, E., García, J., Mendoza, C., et al. 2014, *ApJ*, 790, 131
- Gorczyca, T. W., Bautista, M. A., Hasoglu, M. F., et al. 2013, *ApJ*, 779, 78
- Hasinger, G. & van der Klis, M. 1989, *A&A*, 225, 79
- Henke, B. L., Gullikson, E. M., & Davis, J. C. 1993, *Atomic Data and Nuclear Data Tables*, 54, 181
- Henning, T. 2010, *ARA&A*, 48, 21
- HI4PI Collaboration, Ben Bekhti, N., Flöer, L., et al. 2016, *A&A*, 594, A116
- Hoffman, J. & Draine, B. T. 2016, *ApJ*, 817, 139
- Jaeger, C., Molster, F. J., Dorschner, J., et al. 1998, *A&A*, 339, 904
- Jenkins, E. B. 2009, *ApJ*, 700, 1299
- Jiang, N. & Spence, J. 2006, *Ultramicroscopy*, 106, 215
- Joachim, K., Gattuzi, E., García, J. A., & Kallman, T. R. 2016, *MNRAS*, 461, 352
- Jones, A. P. & Nuth, J. A. 2011, *A&A*, 530, A44
- Juett, A. M. 2004, in *American Astronomical Society Meeting Abstracts*, Vol. 205, *American Astronomical Society Meeting Abstracts*, 41.04

- Kaastra, J. S. 2017, A&A, 605, A51
- Kaastra, J. S., Mewe, R., & Nieuwenhuijzen, H. 1996, in UV and X-ray Spectroscopy of Astrophysical and Laboratory Plasmas, 411–414
- Kaastra, J. S., Raassen, A. J. J., de Plaa, J., & Gu, L. 2018, SPEX X-ray spectral fitting package
- Kaastra, J. S., Raassen, T., & de Vries, C. 2010, in The Energetic Cosmos: from Suzaku to ASTRO-H, 70–73
- Kallman, T. & Bautista, M. 2001, ApJS, 133, 221
- Kemper, F., Vriend, W. J., & Tielens, A. G. G. M. 2004, ApJ, 609, 826
- King, A. R. & Ritter, H. 1999, MNRAS, 309, 253
- Lee, J. 2009, in Chandra’s First Decade of Discovery, ed. S. Wolk, A. Fruscione, & D. Swartz, 58
- Lee, J. C. & Ravel, B. 2005, ApJ, 622, 970
- Leutenegger, M. A., Kühn, S., Micke, P., et al. 2020, arXiv e-prints, arXiv:2003.13838
- Lodders, K. & Palme, H. 2009, Meteoritics and Planetary Science Supplement, 72, 5154
- Madej, O. K., García, J., Jonker, P. G., et al. 2014, MNRAS, 442, 1157
- Madej, O. K., Jonker, P. G., Fabian, A. C., et al. 2010, MNRAS, 407, L11
- Manzorro, R., Celín, W. E., Pérez-Omil, J. A., Calvino, J. J., & Trasobares, S. 2019, ACS Catalysis, 9, 5157
- Mathis, J. S. 1990, ARA&A, 28, 37
- Mathis, J. S. 1998, ApJ, 497, 824
- Mathis, J. S., Rimpl, W., & Nordsieck, K. H. 1977, ApJ, 217, 425
- Mauche, C. W. & Gorenstein, P. 1986, ApJ, 302, 371
- McClintock, J. E., Remillard, R. A., Petro, L. D., Hammerschlag-Hensberge, G., & Proffitt, C. R. 1984, ApJ, 283, 794
- McLaughlin, B. M. & Kirby, K. P. 1998, Journal of Physics B: Atomic, Molecular and Optical Physics, 31, 4991
- Menzel, A., Benzaid, S., Krause, M. O., et al. 1996, Phys. Rev. A, 54, R991
- Mie, G. 1908, Annalen der Physik, 330, 377
- Min, M., Waters, L. B. F. M., de Koter, A., et al. 2007, A&A, 462, 667
- Mondal, A. S., Dewangan, G. C., Pahari, M., & Raychaudhuri, B. 2018, MNRAS, 474, 2064
- Newville, M. 2004, Consortium for Advanced Radiation Sources, University of Chicago (USA)[<http://xafs.org>], 78
- Nittler, L. R., Alexander, O., Gao, X., Walker, R. M., & Zinner, E. 1997, ApJ, 483, 475
- Nuth, Joseph A., I., Rietmeijer, F. J. M., & Hill, H. G. M. 2002, Meteoritics and Planetary Science, 37, 1579
- Olofsson, J., Augereau, J. C., van Dishoeck, E. F., et al. 2009, A&A, 507, 327
- Parratt, L., C.F., H., & 1957, J. E. 1957, Phys. Rev., 105
- Pearson, K. 1901, The London, Edinburgh, and Dublin Philosophical Magazine and Journal of Science, 2, 559
- Pinto, C., Kaastra, J. S., Costantini, E., & de Vries, C. 2013, A&A, 551, A25
- Pinto, C., Kaastra, J. S., Costantini, E., & Verbunt, F. 2010, A&A, 521, A79
- Planck Collaboration. 2011a, A&A, 536, A25
- Planck Collaboration. 2011b, A&A, 536, A26
- Protassov, R., van Dyk, D. A., Connors, A., Kashyap, V. L., & Siemiginowska, A. 2002, ApJ, 571, 545
- Rho, J., Kozasa, T., Reach, W. T., et al. 2008, ApJ, 673, 271
- Rogantini, D., Costantini, E., Zeegers, S. T., et al. 2018, A&A, 609, A22
- Rogantini, D., Costantini, E., Zeegers, S. T., et al. 2019, A&A, 630, A143
- Savage, B. D. & Sembach, K. R. 1996, ARA&A, 34, 279
- Schulz, N. S., Corrales, L., & Canizares, C. R. 2016, ApJ, 827, 49
- Smale, A. P. 1998, ApJ, 498, L141
- Smith, R. G., Sellgren, K., & Brooke, T. Y. 1993, MNRAS, 263, 749
- Smith, R. K. e. a. 2016, in Society of Photo-Optical Instrumentation Engineers (SPIE) Conference Series, Vol. 9905, Proc. SPIE, 99054M
- Stolte, W. C., Lu, Y., Samson, J. A. R., et al. 1997, Journal of Physics B Atomic Molecular Physics, 30, 4489
- van Dishoeck, E. F. 2004, ARA&A, 42, 119
- van Dishoeck, E. F., Helmich, F. P., Schutte, W. A., et al. 1998, in Astronomical Society of the Pacific Conference Series, Vol. 132, Star Formation with the Infrared Space Observatory, ed. J. Yun & L. Liseau, 54
- Watts, B. 2014, Opt. Express, 22, 23628
- Whittet, D. C. B. 2010, ApJ, 710, 1009
- Whittet, D. C. B., Bode, M. F., Longmore, A. J., et al. 1988, MNRAS, 233, 321
- Whittet, D. C. B., Gerakines, P. A., Hough, J. H., & Shenoy, S. S. 2001, ApJ, 547, 872
- Wilms, J., Allen, A., & McCray, R. 2000, ApJ, 542, 914
- Wiscombe, W. J. 1980, Appl. Opt., 19, 1505
- Wooden, D. H., Rank, D. M., Bregman, J. D., et al. 1993, ApJS, 88, 477
- Yao, Y., Schulz, N. S., Gu, M. F., Nowak, M. A., & Canizares, C. R. 2009, ApJ, 696, 1418
- Ysard, N., Köhler, M., Jones, A., et al. 2015, A&A, 577, A110
- Zeegers, S. T., Costantini, E., de Vries, C. P., et al. 2017, A&A, 599, A117
- Zeegers, S. T., Costantini, E., Rogantini, D., et al. 2019, A&A, 627, A16



## Appendix A:

### Dust extinction cross sections in the oxygen K-edge

We present the calculated dust extinction cross sections in the oxygen K-edge. The cross sections were calculated from laboratory data of 18 dust samples with different chemical compositions. The resolution of the laboratory measurements is 0.25 eV.

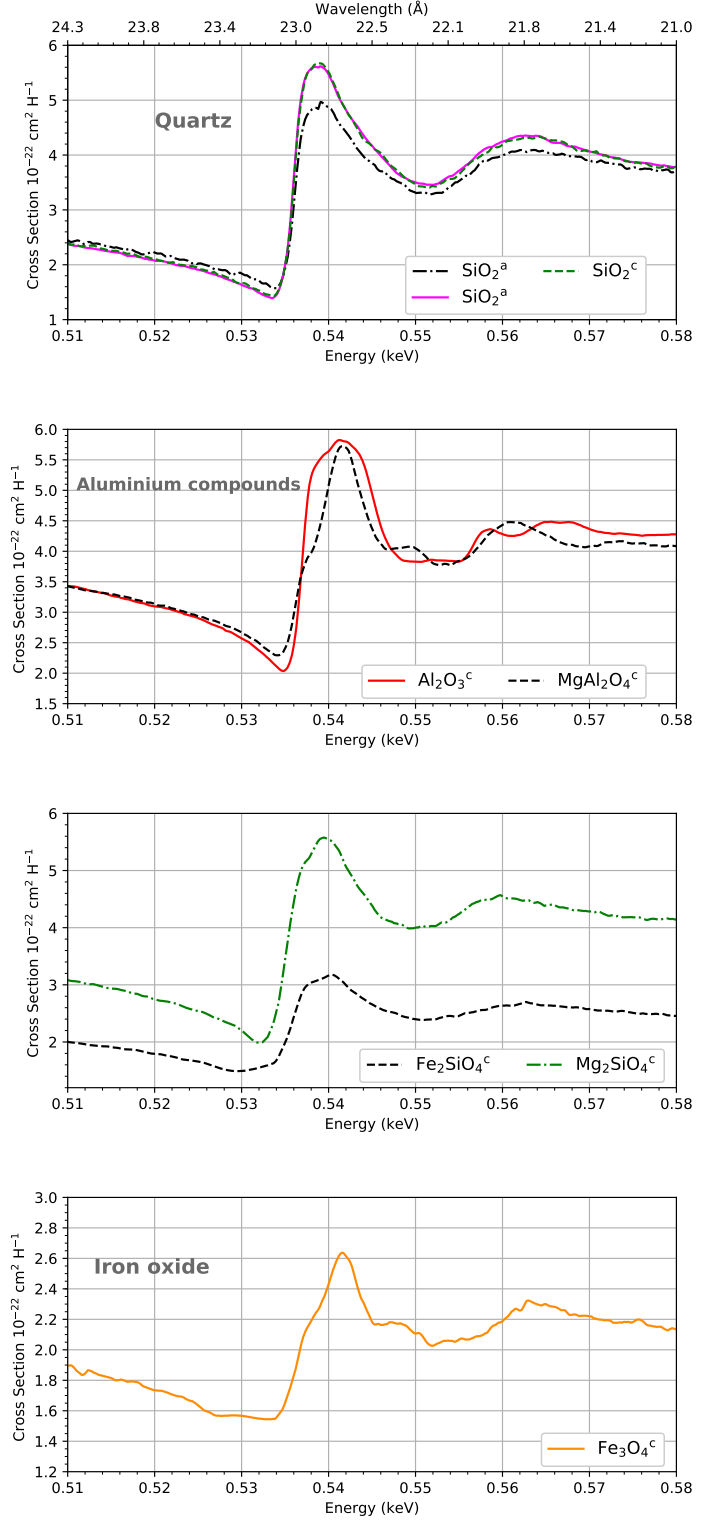
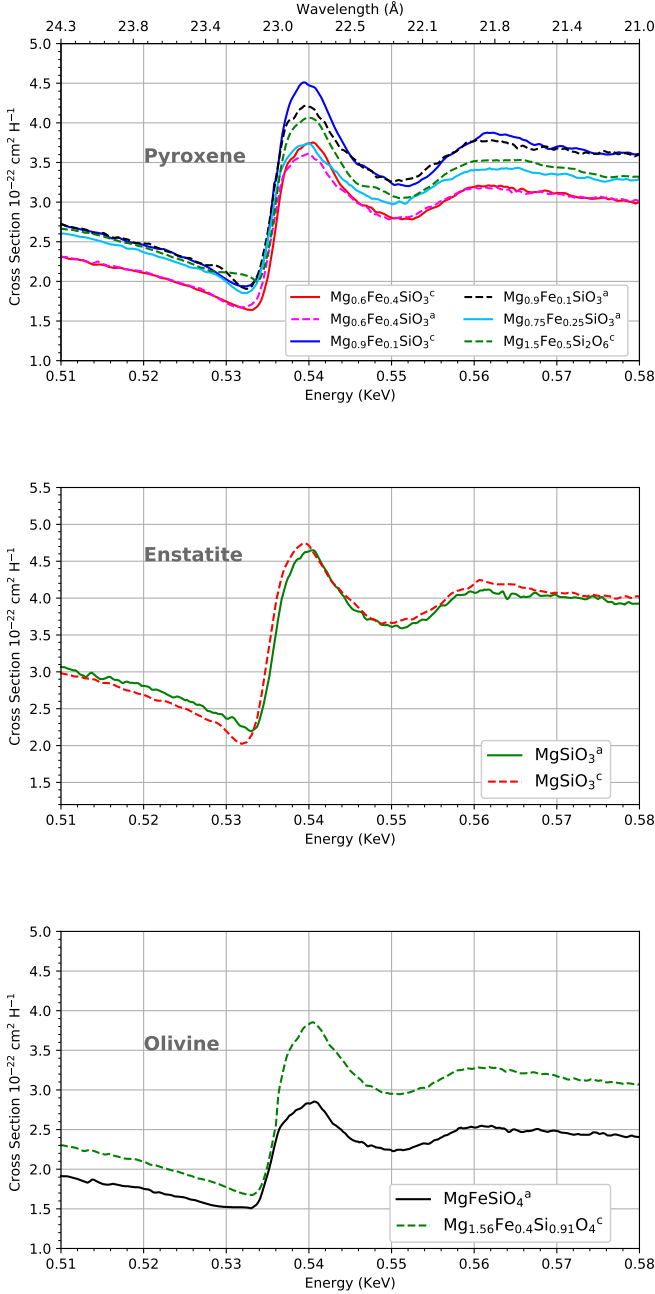


**Fig. A.2.** Calculated dust extinction cross sections. The symbol *a* refers to amorphous compounds and *c* to crystalline.

**Fig. A.1.** Calculated dust extinction cross sections. The symbol *a* refers to amorphous compounds and *c* to crystalline.

**Appendix B: Atomic oxygen lines in SPEX****Table B.2.** O I lines implemented into SPEX

In the following tables we present the wavelength, energy and oscillator strength of the atomic oxygen lines (O I, O II, O III) implemented into SPEX.

**Table B.1.** O I lines implemented into SPEX

$\lambda(\text{\AA})$	E(eV)	$f_{osc}$
22.5760	549.1673	$4.70 \times 10^{-6}$
22.5760	549.1673	$1.03 \times 10^{-5}$
22.5761	549.1648	$6.31 \times 10^{-6}$
22.5772	549.1381	$6.55 \times 10^{-6}$
22.5773	549.1356	$9.08 \times 10^{-6}$
22.5773	549.1356	$1.45 \times 10^{-5}$
22.5778	549.1235	$9.27 \times 10^{-6}$
22.5781	549.1155	$1.32 \times 10^{-5}$
22.5785	549.1075	$2.08 \times 10^{-5}$
22.5788	549.0995	$1.36 \times 10^{-5}$
22.5791	549.0915	$1.95 \times 10^{-5}$
22.5794	549.0835	$3.08 \times 10^{-5}$
22.5798	549.0755	$2.07 \times 10^{-5}$
22.5801	549.0675	$4.88 \times 10^{-5}$
22.5804	549.0596	$3.08 \times 10^{-5}$
22.5808	549.0516	$2.69 \times 10^{-5}$
22.5811	549.0436	$7.50 \times 10^{-5}$
22.5814	549.0356	$4.90 \times 10^{-5}$
22.5817	549.0276	$2.60 \times 10^{-6}$
22.5991	548.6059	$3.58 \times 10^{-6}$
22.6000	548.5841	$4.58 \times 10^{-5}$
22.6003	548.5768	$1.26 \times 10^{-4}$
22.6004	548.5744	$8.36 \times 10^{-5}$
22.6225	548.0385	$8.28 \times 10^{-5}$
22.6234	548.0167	$6.55 \times 10^{-6}$
22.6244	547.9924	$8.32 \times 10^{-6}$
22.6246	547.9876	$1.18 \times 10^{-4}$
22.6247	547.9852	$3.56 \times 10^{-4}$
22.6251	547.9755	$2.59 \times 10^{-4}$
22.6861	546.5020	$4.06 \times 10^{-4}$
22.6904	546.3985	$1.05 \times 10^{-4}$
22.6913	546.3768	$1.59 \times 10^{-4}$
22.6915	546.3720	$5.88 \times 10^{-5}$
22.6922	546.3551	$4.52 \times 10^{-4}$
22.6926	546.3455	$1.22 \times 10^{-3}$
22.7727	544.4238	$4.79 \times 10^{-6}$
22.7735	544.4047	$4.42 \times 10^{-6}$
22.7735	544.4047	$1.79 \times 10^{-5}$
22.7736	544.4023	$2.62 \times 10^{-6}$
22.7736	544.4023	$2.64 \times 10^{-6}$
22.7736	544.4023	$2.53 \times 10^{-6}$
22.7739	544.3951	$4.78 \times 10^{-6}$
22.7740	544.3927	$3.24 \times 10^{-6}$
22.7746	544.3784	$8.22 \times 10^{-5}$
22.7747	544.3760	$1.93 \times 10^{-5}$
22.7748	544.3736	$1.21 \times 10^{-5}$
22.7748	544.3736	$6.07 \times 10^{-6}$
22.7749	544.3712	$8.63 \times 10^{-6}$
22.7749	544.3712	$1.69 \times 10^{-5}$
22.7749	544.3712	$9.12 \times 10^{-6}$

**Notes.**  $\lambda$  and E are the line wavelength and energy, respectively.  $f_{osc}$  is the oscillator strength and it is dimensionless.

$\lambda(\text{\AA})$	E(eV)	$f_{osc}$
22.7756	544.3545	$6.55 \times 10^{-6}$
22.7758	544.3497	$1.11 \times 10^{-5}$
22.7760	544.3449	$6.93 \times 10^{-5}$
22.7761	544.3425	$2.62 \times 10^{-5}$
22.7762	544.3401	$3.06 \times 10^{-5}$
22.7765	544.3330	$3.43 \times 10^{-6}$
22.7766	544.3306	$2.82 \times 10^{-6}$
22.7766	544.3306	$3.83 \times 10^{-6}$
22.7766	544.3306	$4.21 \times 10^{-6}$
22.7777	544.3043	$3.80 \times 10^{-5}$
22.7777	544.3043	$8.45 \times 10^{-5}$
22.7779	544.2995	$4.16 \times 10^{-5}$
22.7789	544.2756	$1.98 \times 10^{-5}$
22.7790	544.2732	$2.27 \times 10^{-6}$
22.7791	544.2708	$7.19 \times 10^{-6}$
22.7792	544.2685	$6.95 \times 10^{-6}$
22.7792	544.2685	$7.73 \times 10^{-6}$
22.7801	544.2470	$1.08 \times 10^{-4}$
22.7802	544.2446	$4.81 \times 10^{-5}$
22.7804	544.2398	$6.03 \times 10^{-5}$
22.7817	544.2087	$6.05 \times 10^{-6}$
22.7822	544.1968	$9.35 \times 10^{-6}$
22.7827	544.1848	$3.33 \times 10^{-5}$
22.7828	544.1825	$2.58 \times 10^{-6}$
22.7830	544.1777	$1.22 \times 10^{-5}$
22.7831	544.1753	$1.41 \times 10^{-5}$
22.7831	544.1753	$1.39 \times 10^{-5}$
22.7839	544.1562	$1.18 \times 10^{-4}$
22.7840	544.1538	$5.50 \times 10^{-5}$
22.7843	544.1466	$9.08 \times 10^{-5}$
22.7873	544.0750	$1.22 \times 10^{-5}$
22.7880	544.0583	$3.84 \times 10^{-5}$
22.7886	544.0440	$3.93 \times 10^{-5}$
22.7889	544.0368	$2.20 \times 10^{-5}$
22.7891	544.0320	$3.51 \times 10^{-5}$
22.7891	544.0320	$2.82 \times 10^{-5}$
22.7896	544.0201	$1.14 \times 10^{-4}$
22.7899	544.0129	$5.20 \times 10^{-5}$
22.7902	544.0058	$1.33 \times 10^{-4}$
22.7976	543.8292	$1.19 \times 10^{-4}$
22.7983	543.8125	$5.00 \times 10^{-4}$
22.7998	543.7767	$6.27 \times 10^{-5}$
22.8001	543.7695	$1.28 \times 10^{-5}$
22.8001	543.7695	$6.65 \times 10^{-5}$
22.8003	543.7648	$1.60 \times 10^{-4}$
22.8006	543.7576	$9.33 \times 10^{-5}$
22.8008	543.7529	$1.22 \times 10^{-4}$
22.8013	543.7409	$4.09 \times 10^{-5}$
22.8015	543.7362	$2.34 \times 10^{-4}$
22.8193	543.3120	$1.18 \times 10^{-4}$
22.8200	543.2954	$5.41 \times 10^{-4}$
22.8233	543.2168	$4.05 \times 10^{-6}$
22.8236	543.2097	$4.01 \times 10^{-4}$
22.8238	543.2049	$1.18 \times 10^{-5}$
22.8240	543.2001	$2.81 \times 10^{-4}$
22.8249	543.1787	$9.06 \times 10^{-4}$
22.8251	543.1740	$4.02 \times 10^{-5}$
22.8258	543.1573	$2.78 \times 10^{-4}$
22.8264	543.1430	$8.49 \times 10^{-6}$
22.8275	543.1169	$2.70 \times 10^{-6}$
22.8754	541.9796	$4.28 \times 10^{-4}$
22.8761	541.9630	$1.55 \times 10^{-3}$
22.8858	541.7333	$1.09 \times 10^{-3}$
22.8882	541.6765	$7.03 \times 10^{-5}$
22.8888	541.6623	$8.73 \times 10^{-4}$
22.8898	541.6386	$4.28 \times 10^{-3}$
22.8931	541.5606	$6.56 \times 10^{-6}$
22.8937	541.5464	$3.99 \times 10^{-5}$
23.5100	527.3501	$3.46 \times 10^{-2}$
23.5114	527.3187	$1.04 \times 10^{-1}$

**Table B.3.** O II lines implemented into SPEX

$\lambda(\text{\AA})$	E(eV)	$f_{osc}$
21.6791	571.8872	$1.59 \times 10^{-4}$
21.6791	571.8872	$2.37 \times 10^{-4}$
21.6992	571.3575	$2.19 \times 10^{-4}$
21.6992	571.3575	$3.24 \times 10^{-4}$
21.6993	571.3548	$1.01 \times 10^{-4}$
21.7183	570.8550	$3.23 \times 10^{-4}$
21.7184	570.8524	$1.08 \times 10^{-4}$
21.7184	570.8524	$2.16 \times 10^{-4}$
21.7353	570.4085	$4.91 \times 10^{-4}$
21.7353	570.4085	$7.29 \times 10^{-4}$
21.7354	570.4059	$2.47 \times 10^{-4}$
21.7399	570.2878	$2.93 \times 10^{-4}$
21.7400	570.2852	$1.88 \times 10^{-4}$
21.7720	569.4470	$3.11 \times 10^{-4}$
21.7722	569.4418	$1.02 \times 10^{-4}$
21.7722	569.4418	$2.05 \times 10^{-4}$
21.8077	568.5148	$1.39 \times 10^{-3}$
21.8078	568.5122	$9.37 \times 10^{-4}$
21.8079	568.5096	$4.72 \times 10^{-4}$
21.8367	567.7598	$1.37 \times 10^{-3}$
21.8368	567.7572	$4.51 \times 10^{-4}$
21.8368	567.7572	$9.07 \times 10^{-4}$
21.9018	566.0722	$3.84 \times 10^{-4}$
21.9020	566.0670	$7.68 \times 10^{-4}$
21.9022	566.0619	$1.13 \times 10^{-3}$
21.9651	564.4409	$3.54 \times 10^{-3}$
21.9653	564.4357	$2.35 \times 10^{-3}$
21.9654	564.4332	$1.17 \times 10^{-3}$
21.9829	563.9838	$6.11 \times 10^{-4}$
21.9831	563.9787	$4.44 \times 10^{-4}$
21.9832	563.9761	$2.32 \times 10^{-4}$
21.9973	563.6146	$4.54 \times 10^{-3}$
21.9974	563.6121	$2.99 \times 10^{-3}$
21.9975	563.6095	$1.49 \times 10^{-3}$
22.0086	563.3252	$1.59 \times 10^{-3}$
22.0086	563.3252	$3.17 \times 10^{-3}$
22.0086	563.3252	$4.75 \times 10^{-3}$
22.0335	562.6886	$1.38 \times 10^{-4}$
22.0335	562.6886	$2.76 \times 10^{-4}$
22.0335	562.6886	$4.15 \times 10^{-4}$
22.0961	561.0945	$1.57 \times 10^{-3}$
22.0961	561.0945	$3.14 \times 10^{-3}$
22.0962	561.0920	$4.71 \times 10^{-3}$
22.2625	556.9006	$1.28 \times 10^{-2}$
22.2625	556.9006	$4.28 \times 10^{-3}$
22.2625	556.9006	$8.55 \times 10^{-3}$
23.3499	530.9659	$3.35 \times 10^{-2}$
23.3506	530.9500	$6.70 \times 10^{-2}$
23.3517	530.9249	$1.01 \times 10^{-1}$

**Table B.4.** O III lines implemented into SPEX

$\lambda(\text{\AA})$	E(eV)	$f_{osc}$
20.7883	596.3932	$1.24 \times 10^{-3}$
20.7956	596.1838	$3.05 \times 10^{-4}$
20.7975	596.1293	$9.58 \times 10^{-4}$
20.8260	595.3136	$2.57 \times 10^{-4}$
20.8286	595.2392	$2.23 \times 10^{-4}$
20.8519	594.5741	$1.36 \times 10^{-3}$
20.8625	594.2720	$5.32 \times 10^{-4}$
20.8646	594.2122	$1.50 \times 10^{-3}$
20.8905	593.4755	$5.66 \times 10^{-4}$
20.8938	593.3818	$7.06 \times 10^{-4}$
20.9735	591.1269	$2.87 \times 10^{-3}$
21.0036	590.2798	$6.80 \times 10^{-3}$
21.0101	590.0971	$1.00 \times 10^{-2}$
21.0280	589.5948	$3.77 \times 10^{-4}$
21.0284	589.5836	$2.63 \times 10^{-4}$
21.0322	589.4771	$1.73 \times 10^{-4}$
21.0784	588.1851	$3.28 \times 10^{-3}$
21.0859	587.9759	$6.38 \times 10^{-3}$
21.0945	587.7361	$1.21 \times 10^{-3}$
21.0957	587.7027	$1.71 \times 10^{-4}$
21.1666	585.7341	$1.11 \times 10^{-3}$
21.2056	584.6569	$4.75 \times 10^{-4}$
21.2066	584.6293	$1.35 \times 10^{-2}$
21.2240	584.1500	$4.84 \times 10^{-3}$
21.2855	582.4622	$2.23 \times 10^{-3}$
21.3140	581.6834	$2.44 \times 10^{-3}$
21.3252	581.3779	$4.79 \times 10^{-3}$
21.3428	580.8985	$3.40 \times 10^{-3}$
21.3584	580.4742	$6.00 \times 10^{-3}$
21.5092	576.4045	$1.33 \times 10^{-2}$
21.5313	575.8129	$2.34 \times 10^{-2}$
21.5836	574.4176	$5.45 \times 10^{-3}$
22.9400	540.4534	$6.89 \times 10^{-2}$
23.0280	538.3880	$1.04 \times 10^{-1}$
23.0710	537.3846	$1.26 \times 10^{-1}$

**Notes.**  $\lambda$  and E are the line wavelength and energy, respectively.  $f_{osc}$  is the oscillator strength and it is dimensionless.